Prediction of Rotor Structural Loads with Comprehensive Analysis

Hyeonsoo Yeo*
Research Scientist
Aeroflightdynamics Directorate (AMRDEC)
U.S. Army Research, Development, and Engineering Command
Ames Research Center, Moffett Field, CA

Wayne Johnson
Research Scientist
Aeromechanics Branch
National Aeronautics and Space Administration
Ames Research Center, Moffett Field, CA

Blade flap and chord bending and torsion moments are investigated for five rotors operating at transition and high speed: H-34 in flight and wind tunnel, SA 330 (research Puma), SA 349/2, UH-60A full-scale, and BO-105 model (HART-I). The measured data from flight and wind tunnel tests are compared with calculations obtained using the comprehensive analysis CAMRAD II. The calculations were made using two free wake models: rolled-up and multiple-trailer with consolidation models. At transition speed, there is fair to good agreement for the flap and chord bending moments between the test data and analysis for the H-34, research Puma, and SA 349/2. Torsion moment correlation, in general, is fair to good for all the rotors investigated. Better flap bending and torsion moment correlation is obtained for the UH-60A and BO-105 rotors by using the multiple-trailer with consolidation wake model. In the high-speed condition, the analysis shows generally better correlation in magnitude than in phase for the flap bending and torsion moments. However, a significant underprediction of chord bending moment is observed for the research Puma and UH-60A. The poor correlation of the chord bending moment for the UH-60A appears to be caused by both the airloads model (at all radial locations) and the lag damper model (mostly at inboard locations).

Nomenclature

A	rotor disk area, πR^2
C_T	rotor thrust coefficient, $T/\rho A(\Omega R)^2$
c	nominal blade chord
M	Mach number
N_b	number of blades
R	blade radius
r	blade radial station
α_{TPP}	tip path plane tilt angle, positive forward
γ	Lock number
μ	advance ratio
ρ	air density
σ	solidity
Ω	rotor rotational speed

Introduction

The accurate prediction of rotor loads and vibration remains a difficult problem for helicopter design. Typically, helicopters encounter high vibration in two different speed regimes: transition and high speed. The rotor blade aerodynamic environment in transition is characterized by blade–vortex interactions (BVI), and in high speed by compressibility and negative loading on the advancing side. The ability to accurately predict the rotor blade loads for these two flight regimes is essential for the design of rotorcraft.

For the past several decades, a number of flight and wind tunnel tests have been conducted to understand the nature of airloads acting on the rotor blade and structural loads due to aerodynamic loading (Refs. 1–6). These extensive flight and wind tunnel data sets provide a valuable resource that can be used to evaluate comprehensive codes' accuracy and reliability and to develop better methodologies to simulate the rotor dynamic response.

Analyses need to provide consistently good predictions for various rotors and flight conditions to be used for design work. The first step to obtain better prediction is to understand the deficiencies of the current analyses. This can be achieved by comparing calculations with flight and wind tunnel measurements for different rotors. Once the deficiencies are identified, effort can be made to improve the methodology.

Reference 7 compared structural measurements from flight and wind tunnel tests of a number of full-scale rotors (H-34, CH-53A, S-76, AH-1G, SA 330, SA 349/2, and UH-60A) at a high-speed condition. It was concluded that the similar load behavior observed among several rotors provides a good test for theoretical methods. The present study examines the blade structural loads at both low and high speeds and compares the analytical methods with experimental measurements.

Reference 8 compared calculated airloads with measured data for the same rotors considered in the present paper. At low speed, the analysis with a rolled-up wake model captured the rapid azimuthal changes of normal force reasonably well for the H-34, research Puma, and SA 349/2. However, the calculated normal force differed significantly from the measurements for the UH-60A and BO-105. Better correlation was obtained for the UH-60A and BO-105 by using a free wake geometry calculation method that combined the multiple-trailer wake with a simulation

*Corresponding author; email: hsyeo@mail.arc.nasa.gov.
Revised paper presented at the 31st European Rotorcraft Forum, Florence, Italy, September 13–15, 2005.
Manuscript received December 2005; accepted February 2008.

of the tip vortex formation process (consolidation). At high speed, the same analysis showed, in general, poor to fair correlation and the effect of wake models was small. As a continuation of the work in Ref. 8, this paper carried out flap and chord bending and torsion moment correlation and focused on the general utility of the multiple-trailer with the consolidation wake model.

The purpose of the present study is to (1) understand the similarities and differences in blade loads among the measurements as well as calculations, (2) use a modern comprehensive code to assess key analytical elements that affect blade loads predictions, and (3) carry out calculations with various wake models and assess the general utility of the multiple-trailer with consolidation wake model.

The calculations were performed using the comprehensive analysis CAMRAD II (Ref. 9).

Test Data

Flight and wind tunnel test cases from various rotors (Refs. 1–6) have been carefully selected so that they represent similar test conditions. Figure 1 and Table 1 show the thrust and advance ratio considered and some of the rotor parameters. The thrust coefficient values range from $C_T/\sigma = 0.057$ to 0.079, and the advance ratios are in the range of $\mu = 0.129$–0.15 at transition, and $\mu = 0.361$–0.39 at high speed.

The flight (Ref. 1) and wind tunnel (Ref. 2) tests of an H-34 helicopter have long been a standard for rotor loads correlation. The blade flap and chord bending and torsion moment data for the H-34 in flight were measured at six radial stations ($r/R = 0.15$, 0.275, 0.375, 0.45, 0.575, and 0.65), three radial stations ($r/R = 0.15$, 0.375, and 0.575), and two radial stations ($r/R = 0.15$, and 0.5), respectively, and were averaged over three consecutive revolutions. Time history data are available with a 15-deg azimuthal step. The structural loads data for the H-34 in the wind tunnel were averaged over 10 revolutions. Harmonic data (up to 10/rev) are available at $r/R = 0.375$ and 0.65, and time history data are available at the other radial stations with a 5-deg azimuthal step.

The research Puma (SA 330) data were obtained using a modified swept-tip blade rather than the standard rectangular Puma blade (Ref. 3). A single revolution of data was taken for each test point; therefore, there is no averaging of data. High-resolution frequency-domain data (up to 126/rev) are available, but the time histories presented in this paper were generated using only the first 60 harmonics.

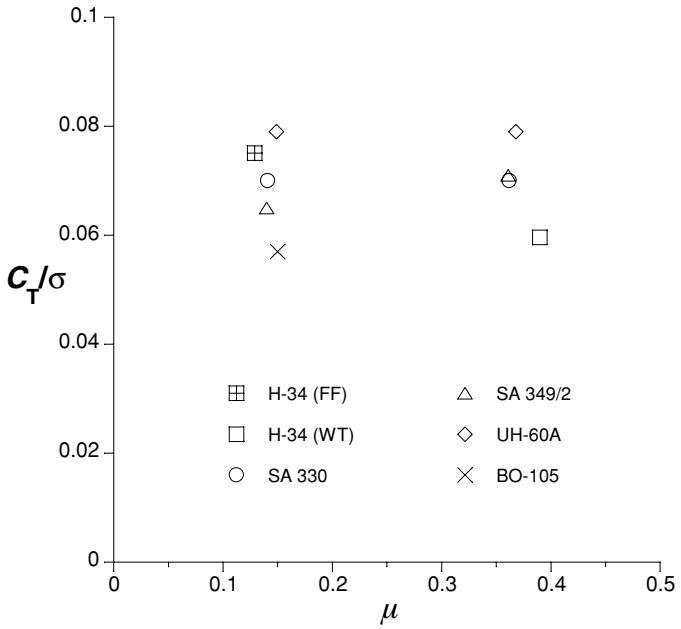

Fig. 1. Rotor thrust coefficient and advance ratio of test data examined.

The SA 349/2 flight data were obtained from an upgraded Gazelle helicopter with three research Grande Vitesse (GV) blades (Ref. 4). Data from each of the strain gauges were acquired over a period of six consecutive rotor revolutions and then averaged. Harmonic data are available up to 10/rev.

Test data with the UH-60A were obtained from the NASA/Army UH-60A Airloads Program (Ref. 5). For this study, a single revolution of data was used from each test point. The data have 7.5 deg azimuthal resolution.

Table 1. Rotor parameters and operating conditions

	H-34	H-34	SA 330	SA 349/2	UH-60A	BO-105
Configuration	Articulated	Articulated	Articulated	Articulated	Articulated	Hingeless
N_b	4	4	4	3	4	4
σ	0.0622	0.0622	0.091	0.0627	0.0826	0.077
Test	flight	wind tunnel	flight	flight	flight	wind tunnel
Radius (inch)	336.0	336.0	296.7	206.7	322.0	78.7
Scale	Full scale	Full scale	Full scale	Full scale	Full scale	Model scale
Low speed						
C_T/σ	0.075		0.070	0.065	0.079	0.057
μ	0.129		0.141	0.140	0.149	0.150
γ	7.8		6.9	4.6	6.4	4.8
α_{TPP} (deg)	4.1		1.3	1.2	0.8	−4.2
$M_{90,tip}$	0.628		0.672	0.719	0.740	0.735
High speed						
C_T/σ		0.060	0.070	0.071	0.079	
μ		0.390	0.362	0.361	0.368	
γ		6.7	6.8	4.1	6.1	
α_{TPP} (deg)		6.0	7.5	7.5	8.0	
$M_{90,tip}$		0.803	0.803	0.872	0.878	

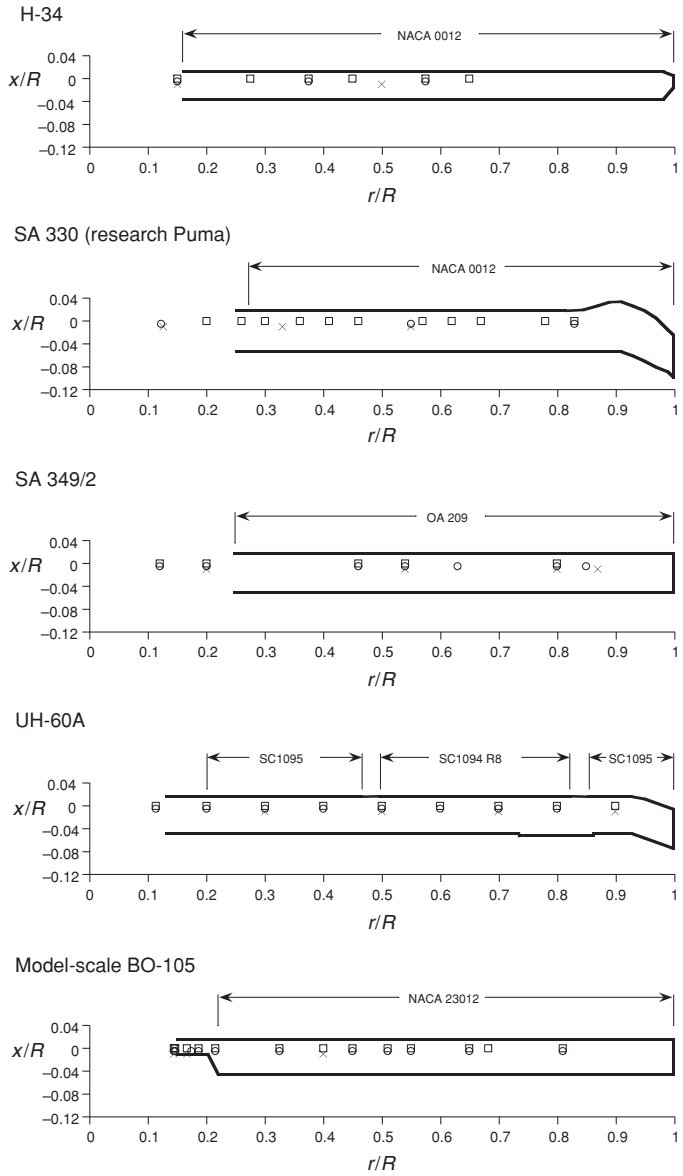

Fig. 2. Blade planforms (□: flap bending, ○: chord bending, and ×: torsion moment measurements).

The BO-105 data were obtained from the Higher-harmonic Acoustics Rotor Test (HART-I) program using a 40% Mach-scaled hingeless BO-105 main rotor blade (Ref. 6). The objective of the test was to demonstrate the reduction of BVI noise in the descending flights using higher harmonic controls. The data set used for the current study is a baseline case without higher-harmonic pitch control inputs. The shaft angle for this condition was 5.3 deg aft (4.2 deg aft when corrected for tunnel wall effects). The structural loads data were averaged over 32 revolutions and filtered to 8 harmonics.

Figure 2 shows the blade planforms for the five rotors, along with the location of the airfoils used and the structural loads measurements.

Analytical Modeling

Rotor trim procedure

The H-34 in flight and wind tunnel, research Puma and UH-60A Black Hawk in flight, and model-scale BO-105 in wind tunnel were modeled in CAMRAD II as isolated rotors. The trim solution for the H-34 in flight and wind tunnel and the research Puma in flight solved for the controls that produced rotor thrust and first harmonic flapping to match the measured values, with the rotor shaft angle of attack fixed at the measured values. Because blade motions were not measured for the BO-105 in wind tunnel, the trim solution was modified to match the measured rotor thrust and hub pitch and roll moments rather than the blade motions.

Both shaft bending moment and blade flapping angle were measured during the NASA/Army UH-60A Airloads program. The hub moment derived from flap angle measurement showed a good agreement with the measured shaft bending moment (Ref. 10), which means the shaft bending moment and 1/rev flap angle measurements are consistent. The trim solution for the UH-60A in flight solved for the controls to match the measured rotor thrust and hub pitch and roll moments (from shaft bending moment).

The SA 349/2 in flight was analyzed as a complete aircraft, with the Fenestron tail rotor modeled as an auxiliary antitorque force. The trim solution for the SA 349/2 in flight solved for the controls and aircraft attitudes that produced zero total force and moment on the aircraft, with zero sideslip angle.

All the calculations were performed without any couplings with the engine/drive train. And, swashplate/hub/fuselage flexibility is also ignored.

Rotor wake modeling

The wake analysis in CAMRAD II calculates the rotor nonuniform induced velocity using the free wake geometry. The concentrated tip vortices are the key features of the rotor wake, important for performance, airloads, structural loads, vibration, and noise calculations. The formation of the tip vortices is modeled in CAMRAD II; it is not calculated from first principles. Two cases are examined here: a rolled-up model and a multiple-trailer with consolidation model. Because of its simplicity and efficiency, the rolled-up model has long been used for helicopter rotors. The multiple-trailer model has also been available, and with the consolidation feature has been applied recently with success to tiltrotor and helicopter airloads calculations (Refs. 8, 11).

The rolled-up wake model is based on the assumption that a tip vortex forms at the blade tip. The bound circulation can have the same sign all along the blade span, or there may be two bound circulation peaks (inboard and outboard peaks of opposite sign). These are the single-peak and dual-peak cases. For the current study, the single-peak model was used for the low-speed conditions, and the dual-peak model was used for the high-speed conditions.

The multiple-trailer model has the far wake trailed vorticity divided into several spanwise panels, to provide more detailed structure for the inboard vorticity, with consolidation of trailed lines in the wake geometry to model the roll-up process. This model has a discrete trailed vortex line emanating from each of the aerodynamic panel edges. The calculation of the free wake geometry includes the distortion of all of these trailed lines. With multiple far wake trailed vorticity panels, the trailed lines at the aerodynamic panel edges can be consolidated into rolled-up lines, using the trailed vorticity moment to scale the rate of roll-up. The trailed vorticity is partitioned into sets of adjacent lines that have the same sign (bound circulation increasing or decreasing). It is assumed that all the vorticity in a set eventually rolls up into a single vortex, located at the centroid of the original vorticity distribution. It should be noted that the computational cost increased by 2–10 times compared to the rolled-up wake model due to the increased number of trailed vortex lines.

Reference 11 has more detailed description on the wake modeling in CAMRAD II.

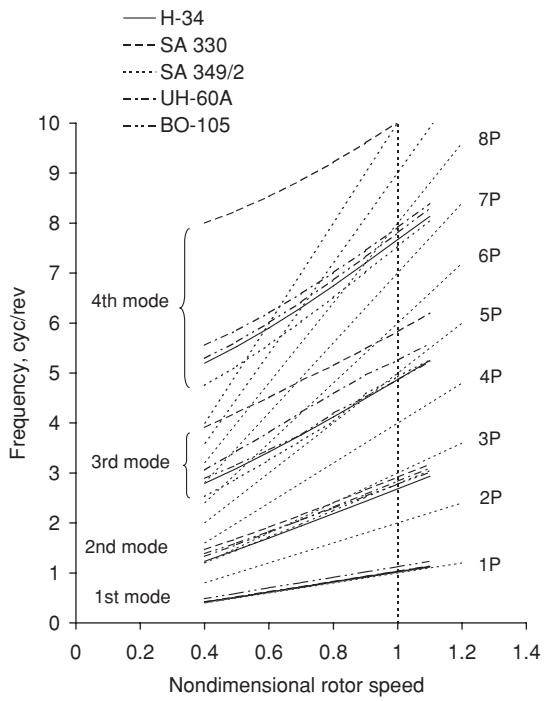

(a) Flap mode frequencies

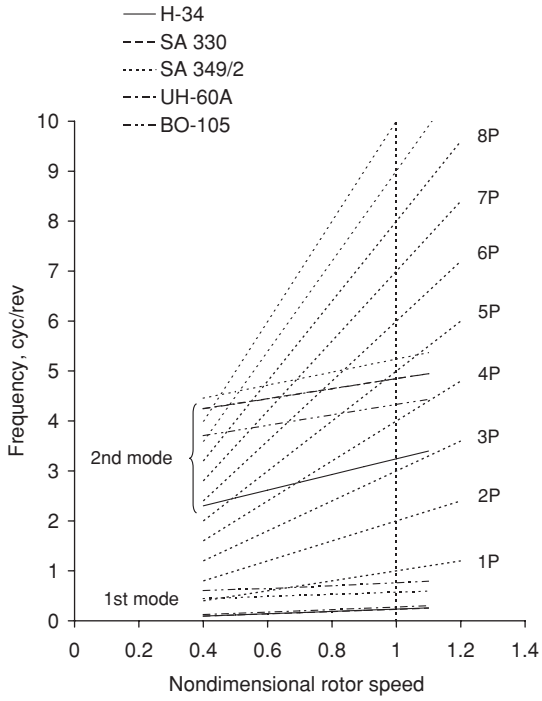

(b) Lag mode frequencies

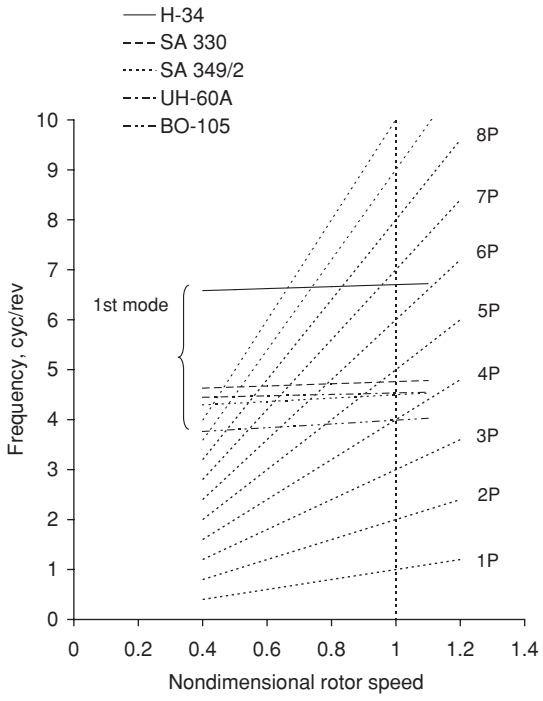

(c) Torsion mode frequencies

Fig. 3. Calculated blade in vacuo frequencies.

Blade Structural Properties

For the accurate calculation of structural loads, it is important to obtain accurate blade structural properties. The structural properties for the H-34, research Puma, and SA 349/2 were obtained from Refs. 2, 3, and 4, respectively. The UH-60A blade properties were obtained from the input database, which has been developed by Yeo and refined over the past years, and has been used extensively for recent studies of UH-60A

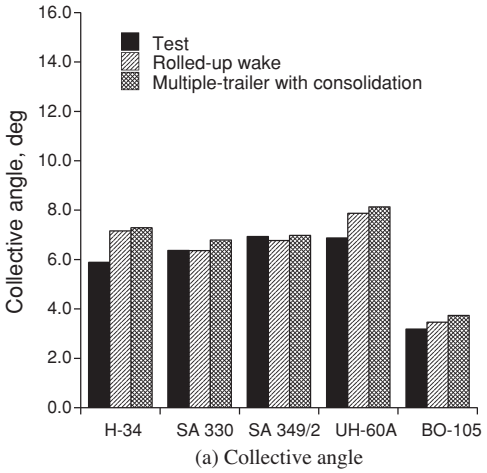

(a) Collective angle

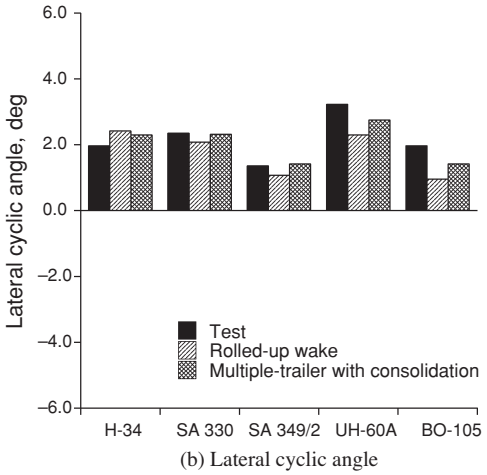

(b) Lateral cyclic angle

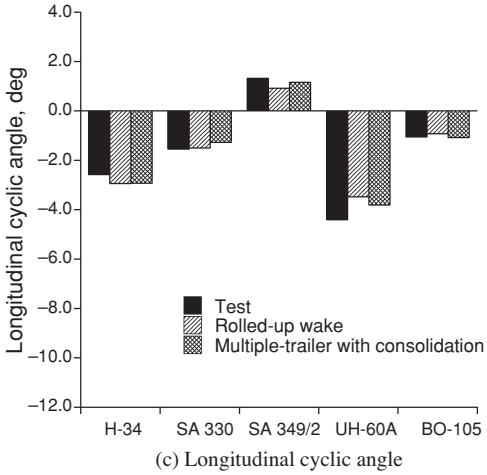

(c) Longitudinal cyclic angle

Fig. 4. Calculated and measured rotor control angles at low speed.

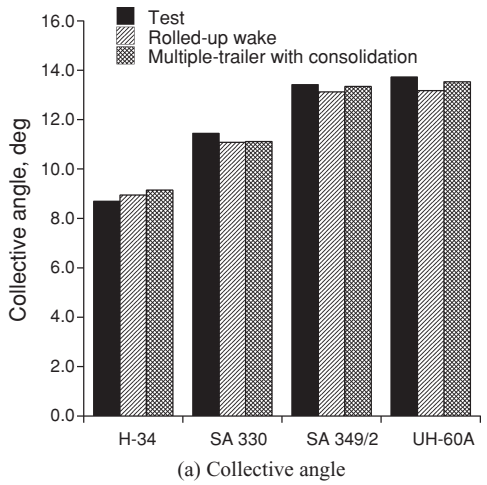

(a) Collective angle

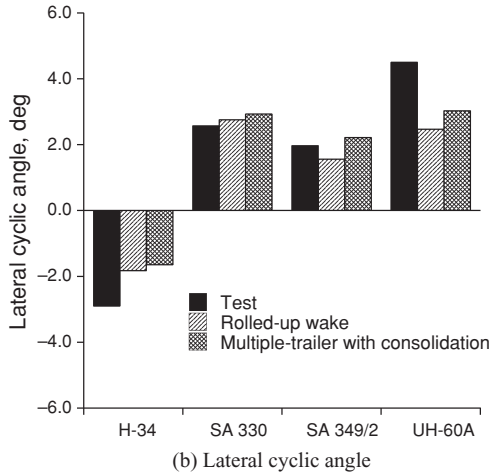

(b) Lateral cyclic angle

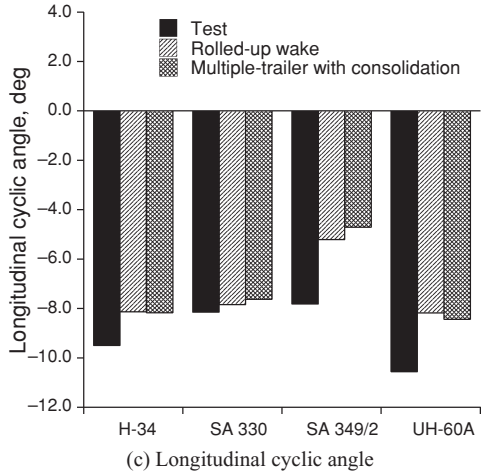

(c) Longitudinal cyclic angle

Fig. 5. Calculated and measured rotor control angles at high speed.

(Refs. 10, 12, 13). As the UH-60 lag damper crosses the coincident flap–lag hinge, its kinematics was fully modeled in three dimensions to capture any damper motions due to flapping. The blade properties for the model-scale BO-105 blade were obtained from the blade manufacturer (DEI Services Corporation). However, the calculated nonrotating natural frequencies did not match the measured values. Thus, the blade flap, chord, and torsion stiffness values were reduced by about 10%, respectively, to match the measured nonrotating natural frequencies. In addition, adjustments were made to the elastic axis and c.g. offset of the blade to obtain better airload correlation.

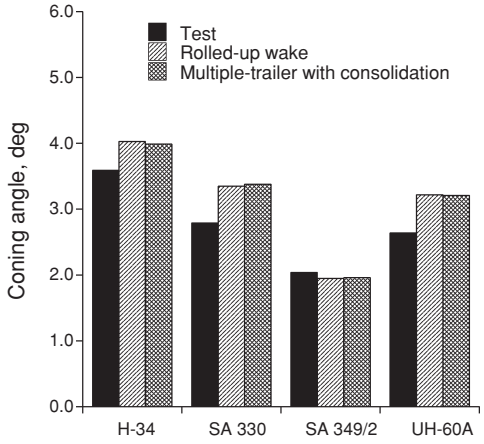

(a) Coning angle

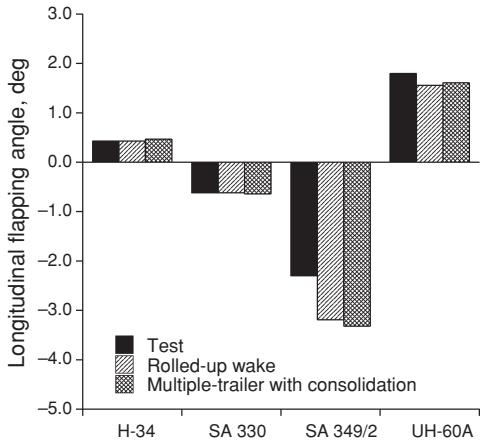

(b) Longitudinal flapping angle

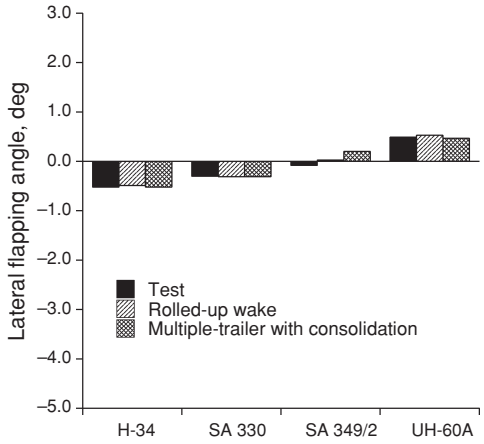

(c) Lateral flapping angle

Fig. 6. Calculated and measured blade flap hinge rotation angles at low speed.

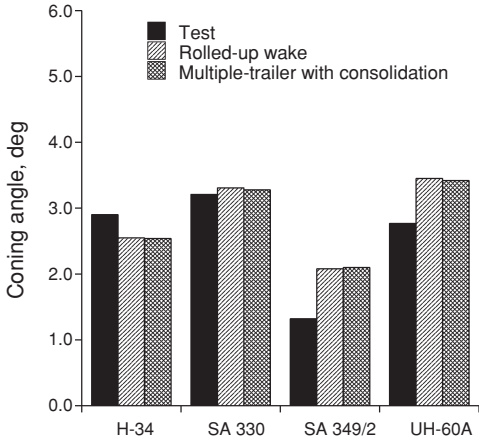

(a) Coning angle

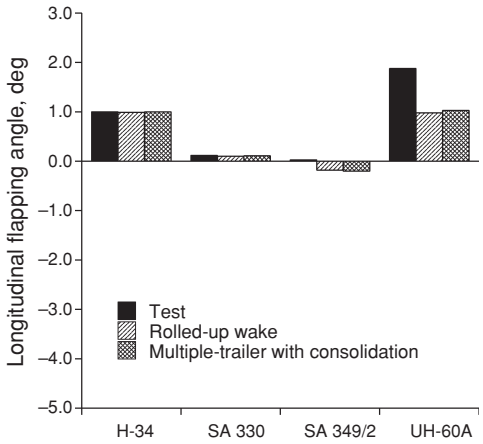

(b) Longitudinal flapping angle

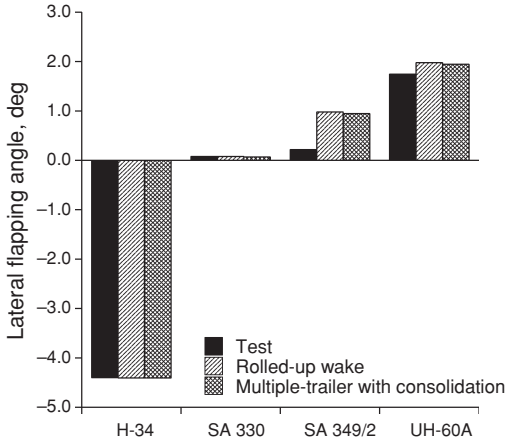

(c) Lateral flapping angle

Fig. 7. Calculated and measured blade flap hinge rotation angles at high speed.

Results and Discussion

The calculated blade flap and chord bending and torsion moments were compared with the flight and wind tunnel measurements. The calculations have been conducted with the identical analysis options for all rotors.

Blade natural frequencies

The blade in vacuo natural frequencies were calculated from 40% to 110% of the nominal rotor speed, and the results are shown in Fig. 3. Measured rotating blade modal data for these rotors could not be obtained; thus, frequency correlation could not be conducted. However,

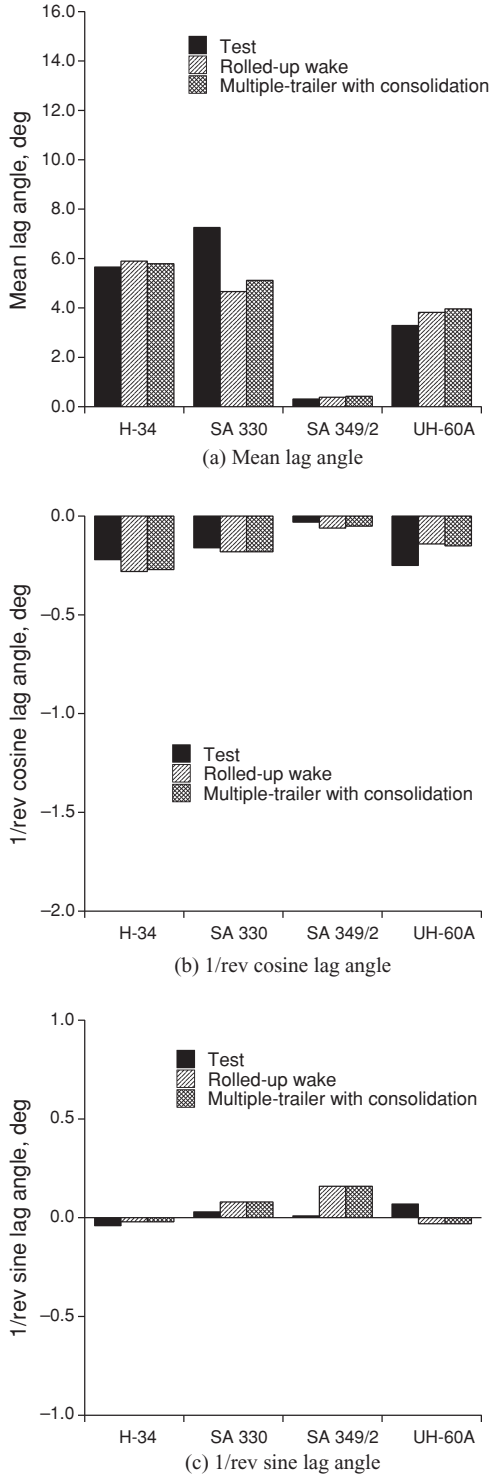

Fig. 8. Calculated and measured blade lag hinge rotation angles at low speed.

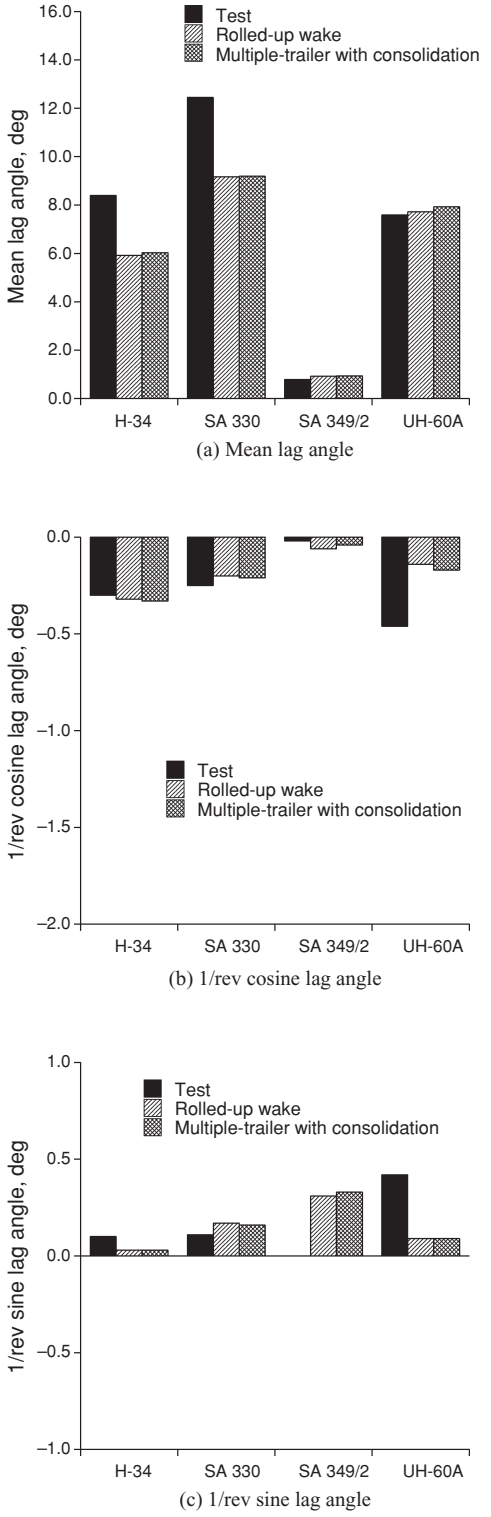

Fig. 9. Calculated and measured blade lag hinge rotation angles at high speed.

the comparison among calculations is still important to understand the similarities and differences in dynamic characteristics of the blades investigated. The first flap frequencies of the articulated rotors (H-34, research Puma, SA 349/2, and UH-60A) range from about 1.02–1.04/rev. The first flap mode frequency of the model-scale BO-105 rotor, which is a hingeless rotor, is higher than those of the articulated rotors. The second flap mode frequencies range from about 2.7 to 2.9/rev, and this is the dominant vibratory flap bending mode for these aircraft. The second flap frequency of the research Puma is closest to 3/rev and that of the H-34 is furthest from 3/rev.

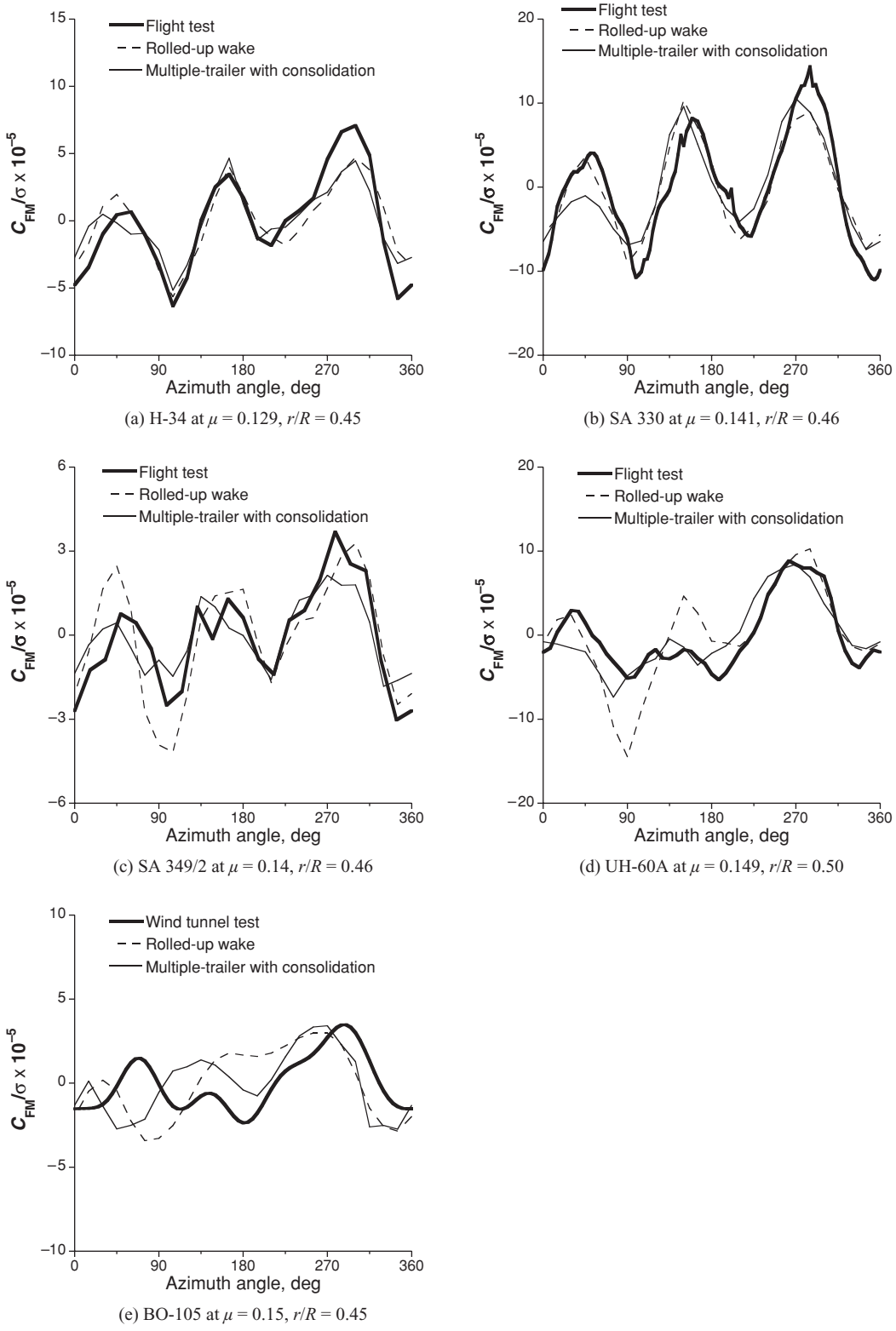

(a) H-34 at $\mu = 0.129$, $r/R = 0.45$

(b) SA 330 at $\mu = 0.141$, $r/R = 0.46$

(c) SA 349/2 at $\mu = 0.14$, $r/R = 0.46$

(d) UH-60A at $\mu = 0.149$, $r/R = 0.50$

(e) BO-105 at $\mu = 0.15$, $r/R = 0.45$

Fig. 10. Calculated and measured blade oscillatory flap bending moment at low speed near $r/R = 0.5$.

All the first chord mode frequencies are below 1/rev. Again, the first chord mode frequency of the model-scale BO-105 rotor, which is a hingeless rotor, is higher than those of the articulated rotors. Considerably more variation is seen in the second chord mode frequencies than was seen in the second flap modes. It should be noted that the calculated second chord mode frequencies of the Research Puma and UH-60A are almost same.

The first torsion frequency of the H-34 is quite high (above 6/rev). The other rotors show first torsion mode frequencies that range from 4/rev to 5/rev.

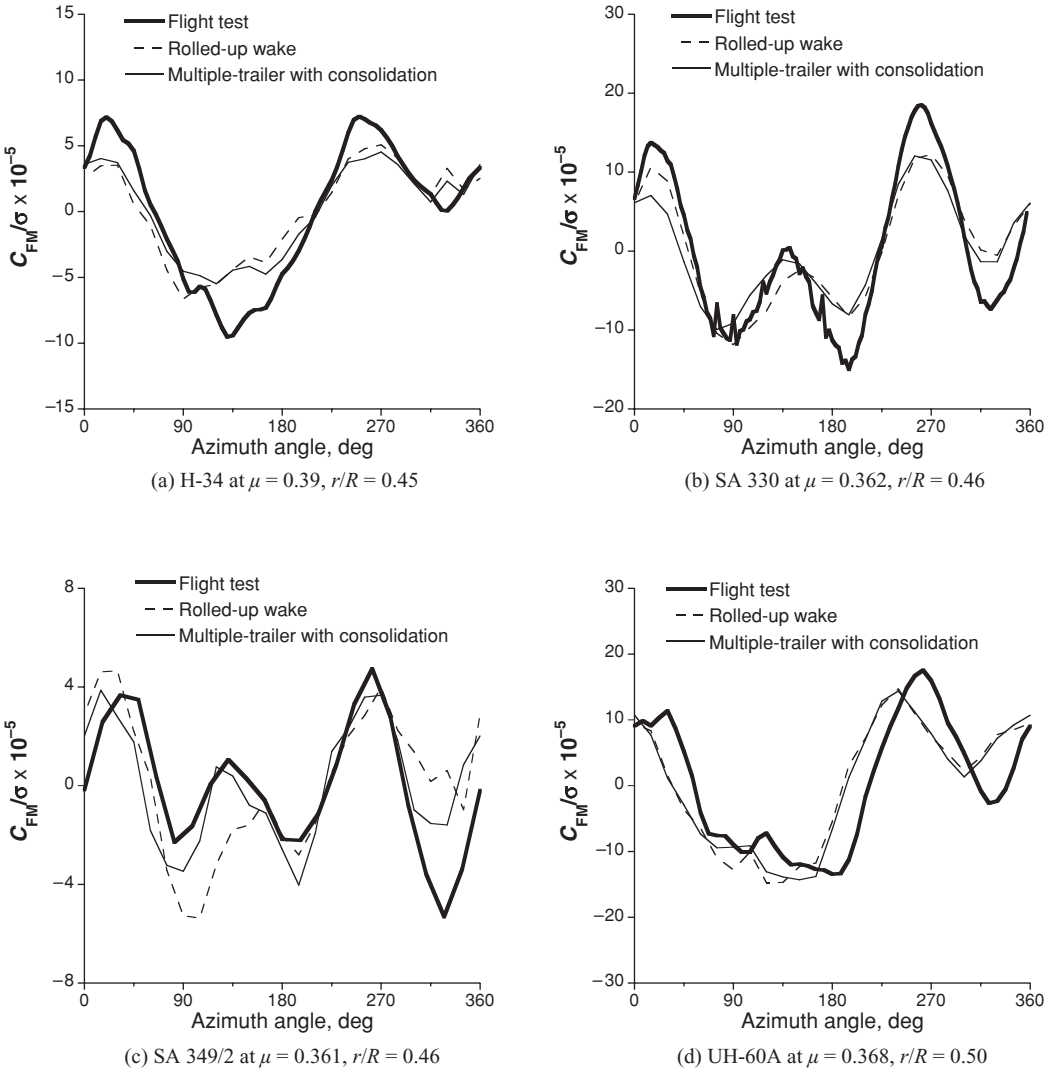

(a) H-34 at $\mu = 0.39$, $r/R = 0.45$

(b) SA 330 at $\mu = 0.362$, $r/R = 0.46$

(c) SA 349/2 at $\mu = 0.361$, $r/R = 0.46$

(d) UH-60A at $\mu = 0.368$, $r/R = 0.50$

Fig. 11. Calculated and measured blade oscillatory flap bending moment at high speed near $r/R = 0.5$.

Trim and blade motion correlation

The trim and blade motion results are investigated in Figs. 4 through 9. Figures 4 and 5 show the calculated and measured rotor control angles at low and high speed, respectively. The measured collective angles are around 6 deg at low speed, except for the model-scale BO-105, and the analysis shows fair to good correlation. The difference between the calculated longitudinal and lateral cyclic angles and measured values is less than 0.9 deg at low speed. The measured collective angles are between 8 and 14 deg at high speed, and the calculation shows good correlation. However, a larger difference is observed in the lateral cyclic angle for the UH-60A and longitudinal cyclic angle for the SA 349/2 and UH-60A. In general, the difference between the two wake models is small for the calculation of control angles.

Figures 6 and 7 compare the calculated flapping angles at the hinge with measured values at low and high speed, respectively. The model-scale BO-105 is of hingeless type; thus, the blade motions at the hinge cannot be compared. Although the first harmonic flapping angles for the H-34 and research Puma were trimmed to match the measured values, the results were included to compare with those of the other rotors. The difference between the calculations and measurements is less than 0.6 deg at low speed and 0.8 deg at high speed. The analysis shows, in general, good correlation for the longitudinal flapping angles, except for the SA 349/2 at low speed, and UH-60A at high speed. The measured lateral flapping angles are very small at low speed, and the analysis predicts them very well. At high speed, the measured lateral flapping angles vary from −4.5 to 2 deg, and the analysis captures the trends, although there is a larger difference for the SA 349/2.

Figures 8 and 9 show the calculated and measured lag angles at the hinge at low and high speed, respectively. The mean lag motions are dominant for all the rotors investigated, and the analysis shows good agreement with measurement for the SA 349/2 and UH-60A. Although a large difference was observed for the SA 330, the lag angle measurement appears to have a bias error of up to −4 deg (Ref. 3). The measured 1/rev lag motions are very small, less than 0.5 deg, and the analysis predicts them well.

Flap bending moment correlation

The measured flap bending moment data from flight and wind tunnel tests were compared with calculations obtained using CAMRAD II.

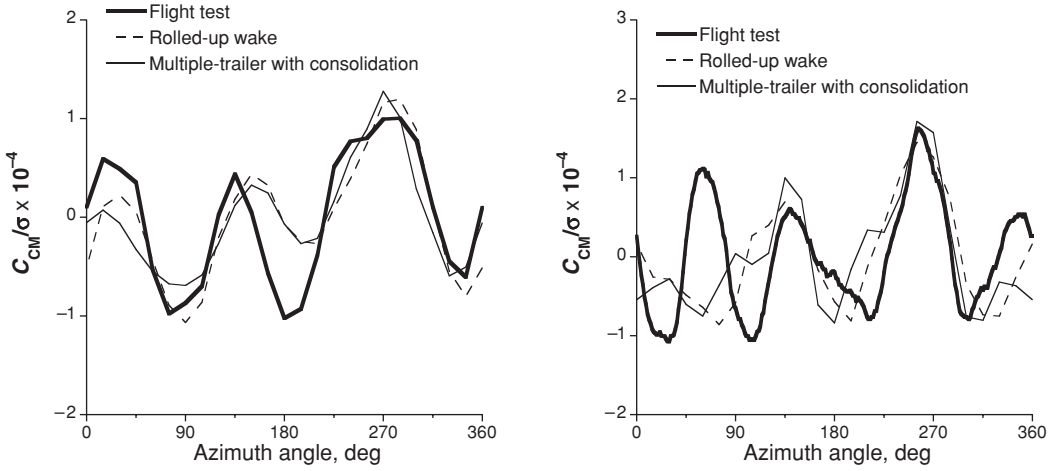

(a) H-34 at $\mu = 0.129$, $r/R = 0.375$

(b) SA 330 at $\mu = 0.141$, $r/R = 0.55$

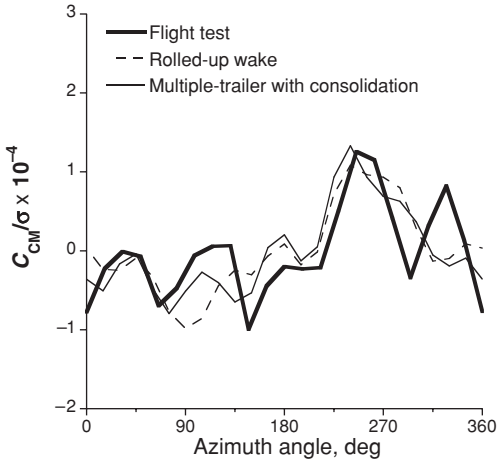

(c) SA 349/2 at $\mu = 0.14$, $r/R = 0.54$

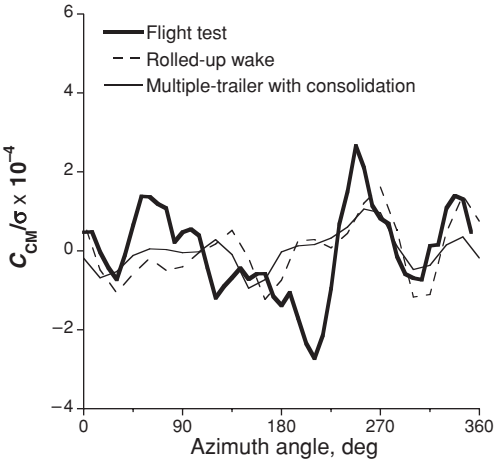

(d) UH-60A at $\mu = 0.149$, $r/R = 0.50$

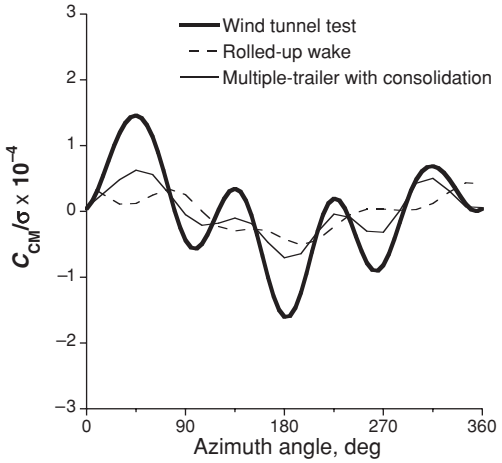

(e) BO-105 at $\mu = 0.15$, $r/R = 0.51$

Fig. 12. Calculated and measured blade oscillatory chord bending moment at low speed near $r/R = 0.5$.

Figure 10 shows nondimensional oscillatory flap bending moments of the H-34, research Puma, SA 349/2, UH-60A Black Hawk, and BO-105 rotors at low speed. Steady values were removed from both test data and analysis. The flap bending moments are shown in the nondimensional form

$$C_{\mathrm{FM}}/\sigma = \frac{M_{\mathrm{F}}}{\rho N_b c \Omega^2 R^4}$$

where M_{F} is the flap bending moment.

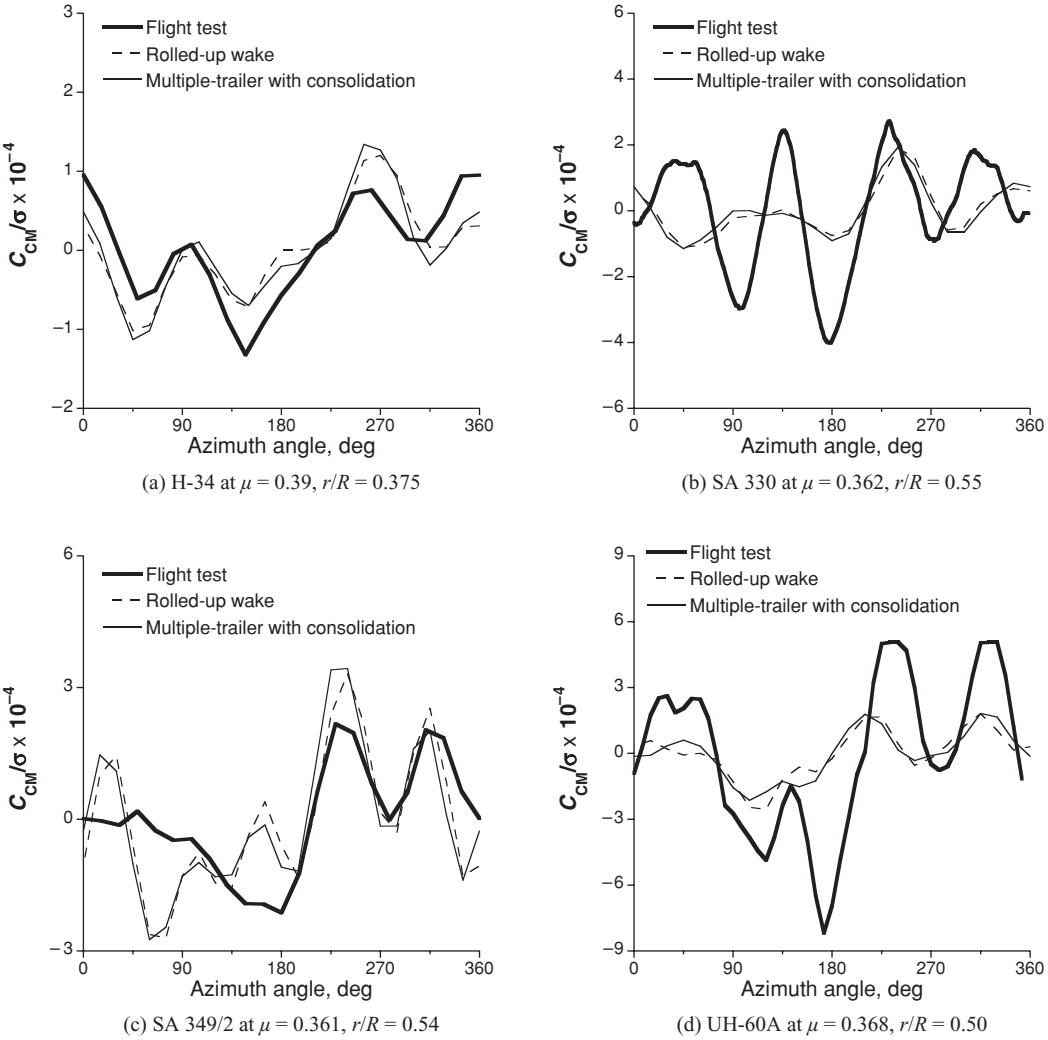

(a) H-34 at $\mu = 0.39$, $r/R = 0.375$

(b) SA 330 at $\mu = 0.362$, $r/R = 0.55$

(c) SA 349/2 at $\mu = 0.361$, $r/R = 0.54$

(d) UH-60A at $\mu = 0.368$, $r/R = 0.50$

Fig. 13. Calculated and measured blade oscillatory chord bending moment at high speed near $r/R = 0.5$.

Calculations were made using two wake models: a rolled-up and a multiple-trailer wake with consolidation. The analysis results were compared with measured data near midspan. The analysis with the rolled-up wake model shows, in general, good correlation in both magnitude and phase for the H-34, research Puma, and SA 349/2. The calculated flap bending moments differ significantly from the measurements for the UH-60A and BO-105.

Better correlation was obtained for the UH-60A by using the multiple-trailer with consolidation wake model. For the BO-105, although the multiple-trailer with consolidation wake model shows a slight improvement on the waveform in the second and third quadrants, the analysis shows poor correlation.

Figure 11 shows nondimensional oscillatory flap bending moments at high speed. The analysis shows fair correlation for the H-34. The research Puma data show the dominant 3/rev loading, and the analysis captures the strong 3/rev loading reasonably well. In general, the correlation for the SA 349/2 is fair to good. For the UH-60A, the calculated flap bending moments show fair correlation on magnitude, but the phase differs significantly from the measurements. Except for the SA 349/2, the multiple-trailer with consolidation model has a small influence on the prediction of flap bending moment at high speed.

Chord bending moment correlation

Figures 12 and 13 show nondimensional oscillatory chord bending moment correlation at low and high speed, respectively. Steady values were removed from both test data and analysis.

At low speed, the analysis shows fair to good correlation for the H-34 and SA 349/2. However, a significant difference between the analysis and measured data was observed for the UH-60A and BO-105, underpredicting the peak-to-peak magnitude. For the research Puma, correlation is good on the retreating side but poor on the advancing side. In general, the influence of wake modeling has a small influence on the prediction of chord bending moment.

At high speed, the analysis shows good correlation for the H-34. For the SA 349/2, correlation is good on the retreating side but poor on the advancing side. Although the test show the dominant 4/rev loading for the research Puma and UH-60A, the analysis was not able to capture the strong 4/rev response, significantly underpredicting the magnitude.

The chord bending moment correlation will be further discussed below.

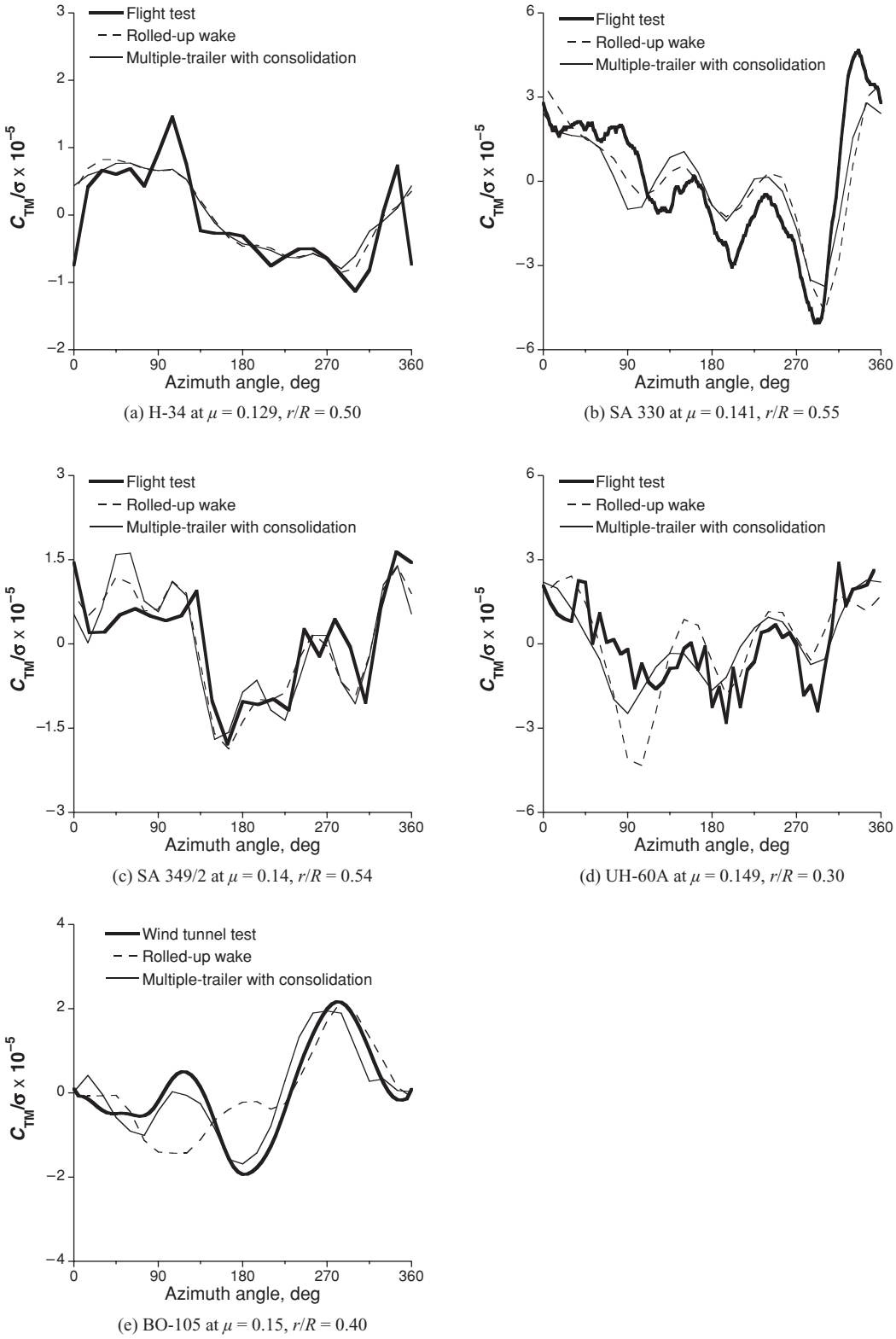

(a) H-34 at $\mu = 0.129$, $r/R = 0.50$

(b) SA 330 at $\mu = 0.141$, $r/R = 0.55$

(c) SA 349/2 at $\mu = 0.14$, $r/R = 0.54$

(d) UH-60A at $\mu = 0.149$, $r/R = 0.30$

(e) BO-105 at $\mu = 0.15$, $r/R = 0.40$

Fig. 14. Calculated and measured blade oscillatory torsion moment at low speed near $r/R = 0.5$.

Torsion moment correlation

Figures 14 and 15 show nondimensional oscillatory torsion moment correlation at low and high speed, respectively. Steady values were removed from both test data and analysis. Most of the first torsion frequencies are between 4/rev and 5/rev for the rotors investigated. However, torsion moments are not dominated by 4/rev or 5/rev. Although the pitching moment correlation, in general, was poor as shown in Ref. 8, the analysis shows fair to good torsion moment correlation at both low and high speeds. Because there is a strong modal coupling between the first

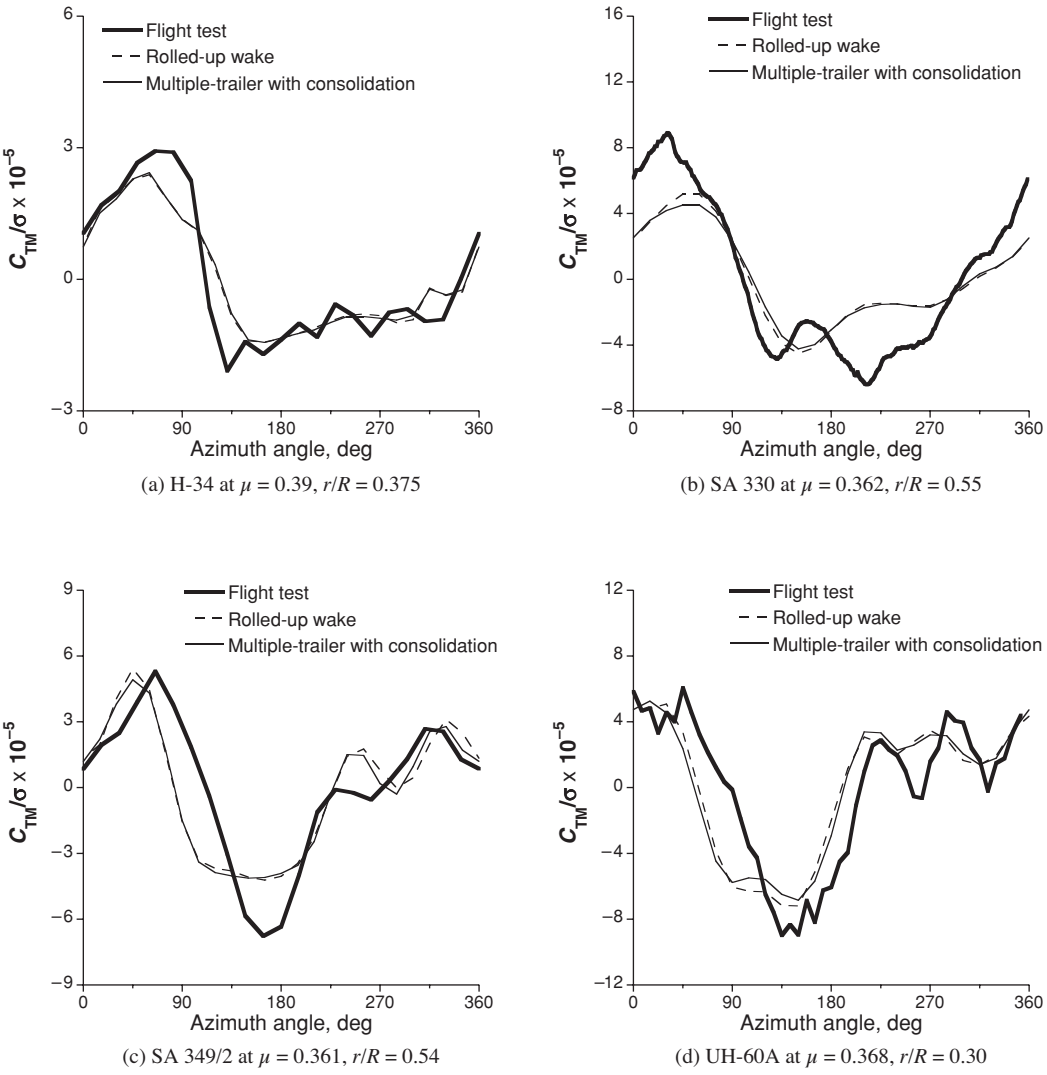

(a) H-34 at $\mu = 0.39$, $r/R = 0.375$

(b) SA 330 at $\mu = 0.362$, $r/R = 0.55$

(c) SA 349/2 at $\mu = 0.361$, $r/R = 0.54$

(d) UH-60A at $\mu = 0.368$, $r/R = 0.30$

Fig. 15. Calculated and measured blade oscillatory torsion moment at high speed near $r/R = 0.5$.

torsion, third flap, and second chord modes, the normal force contribution to the torsion moments appears to be important. Better correlation was obtained for the UH-60A and BO-105 by using the multiple-trailer with consolidation wake model at low speed. Because the multiple-trailer with consolidation wake model improved the airloads on the advancing side of the UH-60A and BO-105 rotors at low speed (Ref. 8), it is consistent that better torsion moment correlation was obtained on the advancing side. A phase difference was still observed in the first and second quadrants for the research Puma and UH-60A.

At high speed, the measured torsion moment shows a strong 1/rev response, which the analysis captures reasonably well. However, a 30-deg phase difference is observed for the SA 349/2 and UH-60A.

Vibratory flap bending moment correlation

Figure 16 shows the vibratory flap bending moments at low speed. Steady, 1/rev, and 2/rev harmonics have been removed from the test data and analyses for the H-34, research Puma, UH-60A, and BO-105. Steady and 1/rev harmonics have been removed for the three-bladed SA 349/2. The harmonics retained are the vibratory loads that are transmitted through the shaft to the fuselage and produce vibration at N_b per rev.

Both the rolled-up and multiple-trailer with consolidation wake models show fair to good correlation for the H-34, research Puma, and SA 349/2. The rolled-up wake model overpredicts the magnitude for the UH-60A. The multiple-trailer with consolidation model tends to reduce the magnitude and thus shows better correlation. Both the rolled-up and multiple-trailer with consolidation wake models show poor to fair correlation for the BO-105.

Figure 17 shows the vibratory flap bending moments at high speed. The analysis shows fair to good correlation for the H-34, research Puma, and SA 349/2. The correlation for the UH-60A is poor. Although the magnitude was reasonably captured, there is a significant phase error.

Further examination of chord bending moment

To understand the poor correlation of the chord bending moment for some of the rotors investigated, the effects of chord stiffness and structural damping were evaluated by looking at arbitrary changes of those

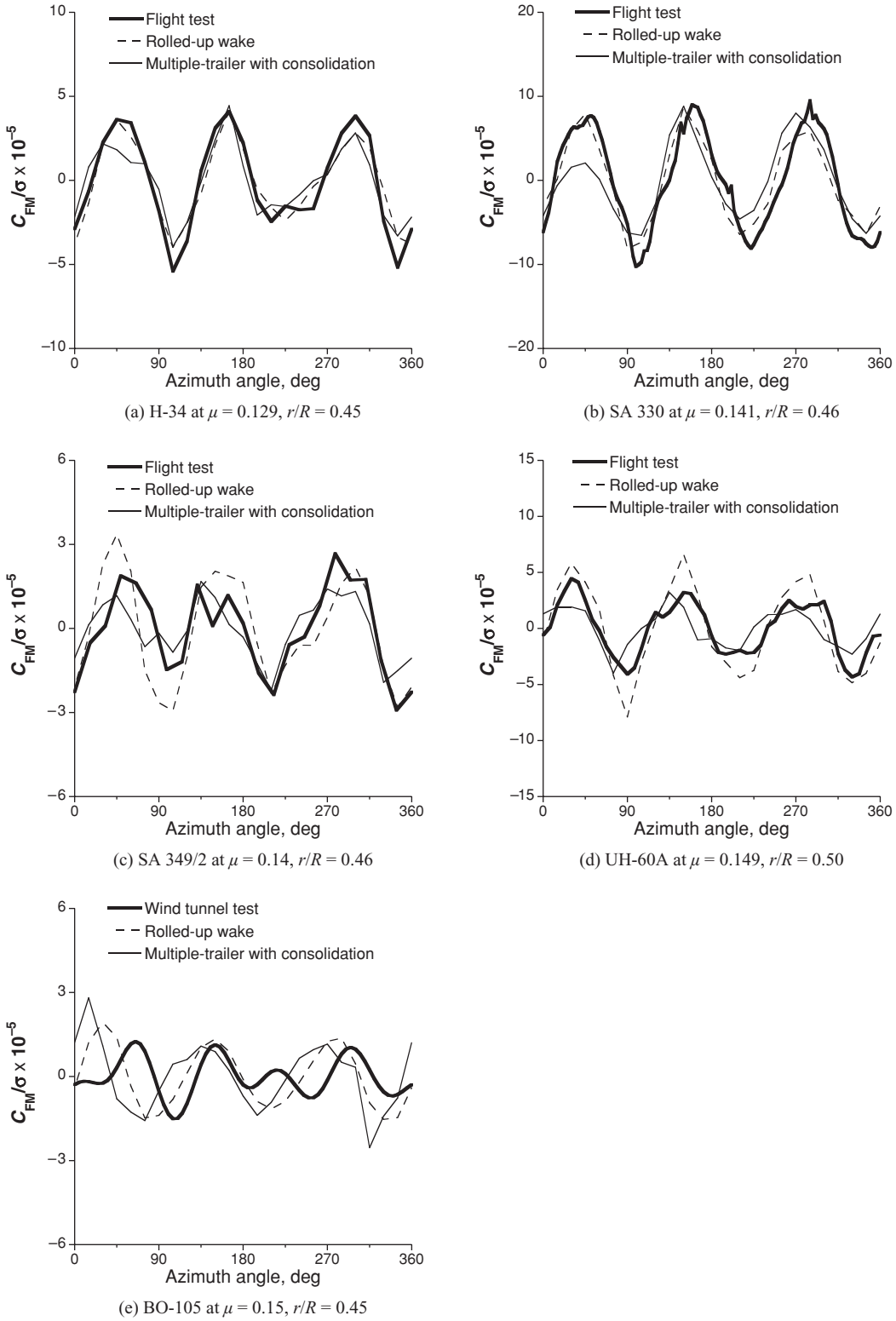

(a) H-34 at $\mu = 0.129$, $r/R = 0.45$

(b) SA 330 at $\mu = 0.141$, $r/R = 0.46$

(c) SA 349/2 at $\mu = 0.14$, $r/R = 0.46$

(d) UH-60A at $\mu = 0.149$, $r/R = 0.50$

(e) BO-105 at $\mu = 0.15$, $r/R = 0.45$

Fig. 16. Calculated and measured blade vibratory flap bending moment at low speed near $r/R = 0.5$.

quantities. This investigation was conducted for the UH-60A in the high-speed condition. Figure 18(a) shows that the effect of chord stiffness on the chord bending moment is small. Because the analysis significantly underpredicted the dominant 4/rev response, the chord stiffness values were reduced to 80%, 60%, and 40% of the baseline chord stiffness to reduce the frequency of the second chord mode. The second chord frequency of the 60% chord stiffness case was 4.04/rev. However, even in that case there was no strong 4/rev response observed. Figure 18(b) shows the effect of variations in structural damping (as equivalent viscous modal damping) of the second chordwise mode on the chord bending moment.

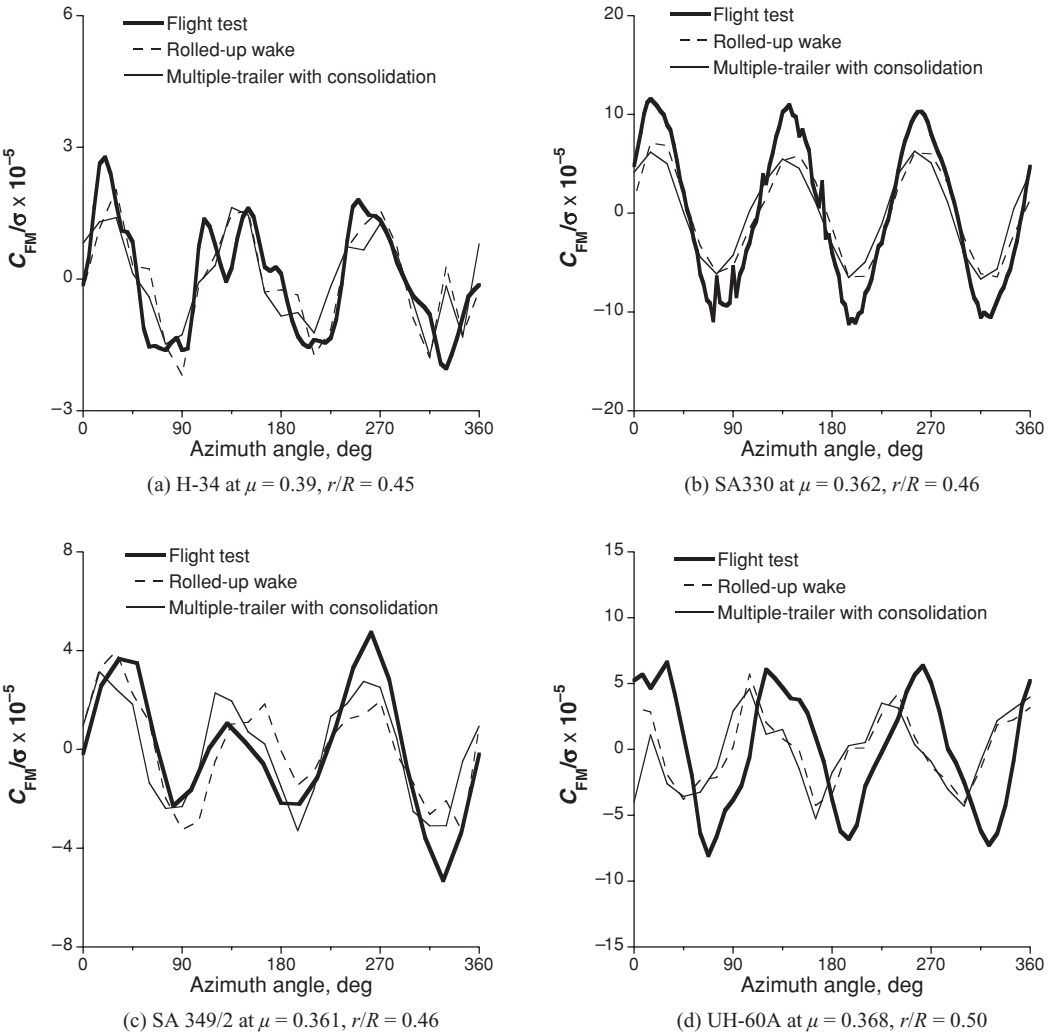

(a) H-34 at $\mu = 0.39$, $r/R = 0.45$

(b) SA330 at $\mu = 0.362$, $r/R = 0.46$

(c) SA 349/2 at $\mu = 0.361$, $r/R = 0.46$

(d) UH-60A at $\mu = 0.368$, $r/R = 0.50$

Fig. 17. Calculated and measured blade vibratory flap bending moment at high speed near $r/R = 0.5$.

The baseline used 0.05% critical modal damping, and the modal damping value was increased to 4% and 8%, respectively. Variations in modal damping had only a small influence on the chordwise bending moment because of the frequency separation between the chordwise natural frequencies and system excitation frequencies.

The rotor blade structural response was calculated using prescribed measured airloads. The pressure data were integrated to obtain normal and chord force and pitching moment. Thus, pressure chord force does not include viscous drag. However, viscous drag has a negligible influence on the chord bending moment calculation. In this way, the rotor structural dynamics problem can be isolated from the rotor aerodynamics problem. Figure 19 shows that the chord bending moment is significantly improved by using the measured airloads at both 50%R and 11.3%R. As a linear lag damper model was used in the baseline calculation, measured lag damper force was prescribed along with the measured airloads. Excellent agreement between the calculations and measurements was obtained at 11.3%R with the measured lag damper force because the chord bending moment is dominated by the lag damper force at this inboard location. Although slightly better results were obtained at 50%R with the measured lag damper force, the effect of measured damper force is much less significant at this radial station. The poor correlation of the chord bending moment appears to be caused by both the airloads model (at all radial locations) and the lag damper model (mostly at inboard locations).

Conclusions

Blade flap and chord bending and torsion moments were investigated for various rotors operating at transition and high speeds: H-34 in flight and wind tunnel, SA 330 (research Puma), SA 349/2, UH-60A full-scale and BO-105 model (HART-I). The H-34, research Puma, SA 349/2, UH-60A data represent steady, level flight conditions and the BO-105 data represent a descending flight condition. Measured data from flight and wind tunnel tests were compared with calculations obtained using the comprehensive analysis CAMRAD II.

From this study the following conclusions were obtained:

Low speed

1) The analysis with a rolled-up wake model shows good flap bending moment correlation for the H-34, research Puma, and SA 349/2. The calculated flap bending moments differ significantly from the measurements for the UH-60A and BO-105.

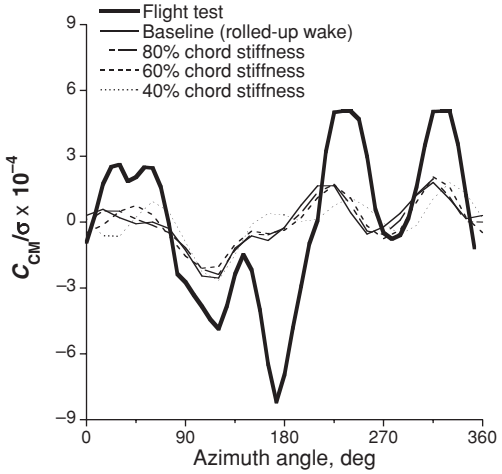

(a) Effect of lag stiffness

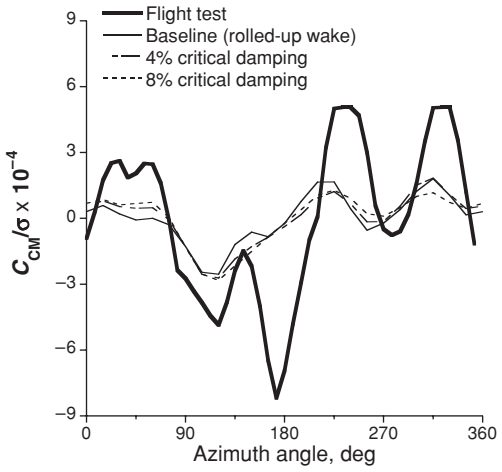

(b) Effect of structural damping

Fig. 18. Chord bending moment for UH-60A at $\mu = 0.368$, $r/R = 0.50$.

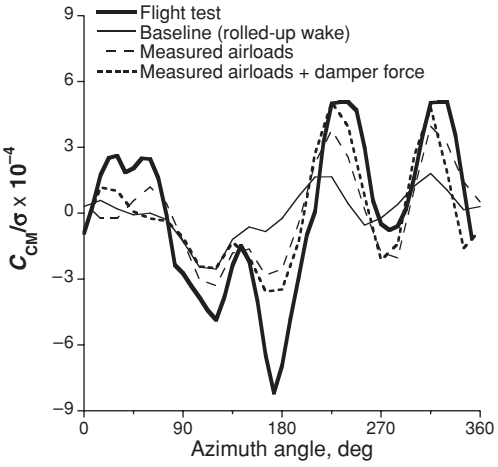

(a) $r/R = 0.50$

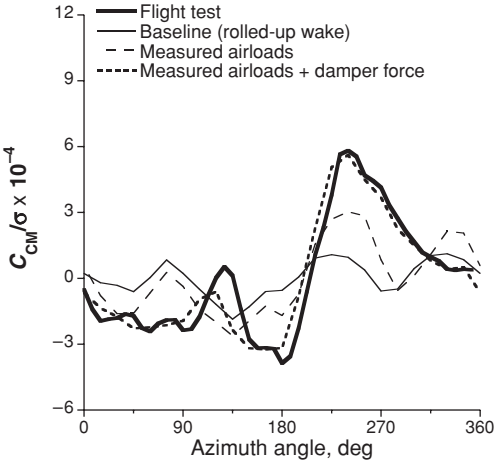

(b) $r/R = 0.113$

Fig. 19. Effect of prescribed measured airloads and damper force on chord bending moment for UH-60A at $\mu = 0.368$.

2) Better flap bending moment correlation is obtained for the UH-60A by using the multiple-trailer with consolidation wake model. However, differences remain between the measurement and analysis.

3) Although the multiple-trailer with consolidation wake model shows good correlation on the normal force for the BO-105 (Ref. 8), the same analysis shows poor correlation on the flap bending moment.

4) The analysis shows fair to good chord bending moment correlation for the H-34 and SA 349/2, but significantly underpredicts peak-to-peak magnitude for the UH-60A and BO-105. For the research Puma, correlation is good only on the retreating side.

5) The wake modeling has a small influence on the calculation of chord bending moment.

6) The torsion moment correlation is quite satisfactory for all the rotors investigated, although aerodynamic pitching moment correlation, in general, was poor (Ref. 8). Better correlation is obtained for the UH-60A and BO-105 by using the multiple-trailer with consolidation wake model.

High speed

7) Measured vibratory flap bending moments show strong 3/rev response at both low and high speed and those are dominated by the second flap bending mode.

8) The analysis shows fair to good oscillatory flap bending moment correlation for the H-34, research Puma, and SA 349/2 and poor phase correlation for the UH-60A.

9) The chord bending moment correlation is good for the H-34 and fair for the SA 349/2. The calculated chord bending moments differ significantly from the measurements for the research Puma and UH-60A.

10) The effect of the chord bending stiffness and structural damping on the predicted chord bending moment is small. The poor correlation of the chord bending moment for the UH-60A appears to be caused by both the airloads model (at all radial locations) and the lag damper model (mostly at inboard locations).

11) The measured torsion moment shows a strong 1/rev response, which the analysis captures reasonably well. However, a 30-deg phase difference is observed for the SA 349/2 and UH-60A.

References

[1]Scheiman, J., "A Tabulation of Helicopter Rotor-Blade Differential Pressures, Stresses, and Motions as Measured in Flight," NASA TM X-952, 1964.

[2]Rabbott, J. P., Jr., Lizak, A. A., and Paglino, V. M., "A Presentation of Measured and Calculated Full-Scale Rotor Blade

Aerodynamic and Structural Loads," USAAVLABS TR 66-31, 1966.

[3]Bousman, W. G., Young, C., Gilbert, N. E., Strawn, R. C., Miller, J. V., Maier, T. H., Costes, M., and Beaumier, P., "A Comparison of Lifting-Line and CFD Methods with Flight Test Data from a Research Puma Helicopter," NASA TM 110421, October 1996.

[4]Heffernan, R. M., and Gaubert, M., "Structural and Aerodynamic Loads and Performance Measurements of an SA 349/2 Helicopter with an Advanced Geometry Rotor," NASA TM 88370, November 1986.

[5]Kufeld, R. M., Balough, D. L., Cross, J. L., Studebaker, K. F., Jennison, C. D., and Bousman, W. G., "Flight Testing of the UH-60A Airloads Aircraft," American Helicopter Society 50th Annual Forum Proceedings, Washington, DC, May 11–13, 1994.

[6]Splettstoesser, W. R., Heller, H., Mercker, E., Preisser, J. S., and Yu, Y. H., "The HART Programme, a Quadrilateral Cooperative Research Effort," American Helicopter Society 51st Annual Forum Proceedings, Ft. Worth, TX, May 9–11, 1995.

[7]Bousman, W. G., "The Response of Helicopter Rotors to Vibratory Airloads," *Journal of the American Helicopter Society*, Vol. 35, (4), October 1990, pp. 53–62.

[8]Yeo, H., and Johnson, W., "Assessment of Comprehensive Analysis Calculation of Airloads on Helicopter Rotors," *Journal of Aircraft*, Vol. 42, (5), September–October 2005, pp. 1218–1228.

[9]Johnson, W., "Technology Drivers in the Development of CAMRAD II," American Helicopter Society Aeromechanics Specialist Conference, San Francisco, CA, January 19–21, 1994.

[10]Yeo, H., Bousman, W. G., and Johnson, W., "Performance Analysis of a Utility Helicopter with Standard and Advanced Rotors," *Journal of the American Helicopter Society*, Vol. 49, (3), July 2004, pp. 250–270.

[11]Johnson, W., "Influence of Wake Models on Calculated Tiltrotor Aerodynamics," American Helicopter Society Aerodynamics, Acoustics, and Test and Evaluation Technical Specialists' Meeting, San Francisco, CA, January 23–25, 2002.

[12]Ormiston, R., "An Investigation of the Mechanical Airloads Problem for Evaluating Rotor Blade Structural Dynamics Analysis," AHS Fourth Decennial Specialists' Conference on Aeromechanics, San Francisco, CA, January 21–23, 2004.

[13]Datta, A., and Chopra, I., "Validation and Understanding of UH-60A Vibratory Loads in Steady Level Flight," *Journal of the American Helicopter Society*, Vol. 49, (3), July 2004, pp. 271–287.